Effect of growth-time on electrochemical performance of birnessite manganese oxide (δ-MnO_2) as electrodes for supercapacitors: An insight into neutral aqueous electrolytes

Kabir O. Oyedotun, Abdulmajid A. Mirghni, Oladepo Fasakin, Delvina Japhet Tarimo, Badr A. Mahmoud and Ncholu Manyala*.

Department of Physics, Institute of Applied Materials, SARChI Chair in Carbon Technology and Materials, University of Pretoria, Pretoria 0028, South Africa.

*Corresponding author's email: ncholu.manyala@up.ac.za, Tel.: + (27)12 420 3549.

ABSTRACT

This study demonstrates successful synthesis of nanoflower-like birnessite δ-MnO_2 materials through a simple and effective hydrothermal technique. Characterization of the flower-like materials grown at various dwell times were carried out by employing scanning electron microscopy (SEM), X-ray diffractometry (XRD), Brunauer-Emmett-Teller (BET) and Barrett–Joyner–Halenda (BJH) models, and electrochemical analysis to understand the effect of different growth time on their morphological, structural, surface area along with pore size distribution and electrochemical characteristics as electrodes for electrochemical capacitors. Attention is mainly based on electrochemical assessment of the as-synthesized materials with an insight into some neutral aqueous electrolytes, mainly lithium sulphate (1 M Li_2SO_4) and sodium sulphate (1 M Na_2SO_4) solutions as potential medium owing to their non-corrosive nature, cost-effectiveness, electrochemical stability and environmentally friendliness. Significant charge propagation, with a high specific capacitance of 387.1 F g^{-1} was achieved for the half-cell electrode in 1 M Li_2SO_4 alongside excellent cycling stability for up to 5 000 cycles performed at 3 A g^{-1} specific current. A comprehensive electrochemical assessment is performed to understanding the relationship

between solvated and diffused ions of the neutral electrolytes that could result in fast charge storage kinetics as well as high specific capacitance.

KEYWORDS: MnO_2; growth-time; morphology; specific capacitance; electrochemical properties.

1. INTRODUCTION

The fast growth in world economy and the population has called for a significant rise in demand for energy consumption. As a result of threats being posed by the harsh influence of fossil fuels on our environment, alongside the incessant rise in call for grid energy storage as well as consumer electronic devices, thus efficient storage systems for energy are highly of yearning effect [1–6]. Electrochemical energy storage devices like supercapacitors and batteries have found their usefulness in compact electronic gadgets as well as in hybrid vehicles/hybrid electric vehicles [7–9] in recent times.

Energy storage devices like supercapacitors (SCs) are of much greater capacitance but suffer lower operational potentials compared to the typical capacitors. SC appears to bridge the gap between the typical capacitors and their batteries counterparts. Such batteries are lithium and sodium ion batteries among others. Supercapacitor presents more energy capability against the traditional capacitors. It is able to accept and supply charges more rapidly, and endure much longer charge and discharge cycles compared to the batteries [10]. The energy storage mechanism in supercapacitors (SCs) majorly comprises charge collection in electrical double layer. A process whose representative electrostatic sort enables SCs to charge and discharge in a matter of seconds and for thousands of cycles[1]. Thus, the devices are typified by high power capabilities and are gainfully applicable in systems such as hybrid electric vehicles (HEV) for

swift and high power delivery in acceleration covering, airplanes as emergency landing systems and/or as possible power sources in city trams [2]. As an attractive choice for electrochemical energy storage owing to their longer cycling lifetimes and higher power densities than rechargeable lithium ion batteries. With the continuous increase in the consumption of portable and wearable electronic devices, supercapacitors have been generating considerable attention recently because of their notable features, such as lightweight, environment friendliness, and good mechanical properties [11–13]. They also serve as great protectors in portable electronic gadgets, which include mobile phones, digital cameras and laptops, owing to their ability to be easily discharged at high current regimes. Nonetheless, SCs still endure low energy capabilities when compared to their commercial lithium-ion batteries counterparts [14,15] that have considerably restricted their farther applications as first-hand sources of power. Past works have revealed that the possibility and improvement of electrode materials could have a huge influence on the pragmatic application of SCs.

Supercapacitors are an auspicious technology as energy storage devices, and later development of viable electrode materials is analytical to developing the devices [16]. As a kind of charge mechanism storage, the capability of its configuration relies on the basic properties of the materials in the device. Transition metal oxides (TMOs) or hydroxides besides conducting polymers have been greatly studied as active materials as electrodes for supercapacitors due to their high theoretical specific capacitances emanating from the fast and reversible faradaic reactions [17] . Today, owing to superb chemical stability, prolific valences, and great electrochemical accomplishment, varying TMOs have been prospects in this field [18–22]. TMO such as RuO_2 is a conductive metal oxide, with variable oxidation states attainable within 1.4 V, presenting a spectacular reported specific capacitance around 2000 F g^{-1} [23]. RuO_2 is familiar as the most potent material, but the high cost and toxicity are restricting its potential for

electrode applications [24]. Thus, more cost-effective TMOs, like manganese oxides, cobalt oxides, nickel oxides and iron oxides, are being considered as promising electrode materials for supercapacitors and established to show rich electrochemical performances. Such TMOs integrates the merits of batteries and electric double-layer capacitors to provide considerable electrochemical capacitances and energy densities. Among these materials, MnO_2 has attracted tremendous interest owing to its abundance, cost effectiveness, low toxicity, variable oxidation states and high theoretical capacitance [25–27]. Supercapacitor (SC), otherwise referred to as electrochemical capacitor (EC), has gained a massive attention due to its high power and high rate capability, long-term cycling, and wide temperature range/safe operation [28,29].

Supercapacitor is a high-capacitance/capacity energy storage device with capacitance values much higher with very low equivalent series resistance and very low leakage to manage pulse requirements compared to the conventional capacitors. The device bridges the gap between the electrolytic capacitors and storage batteries such as lithium ion batteries. It charges and discharges very fast and is able to achieve large amount of cycles [22].

The active material adopted in the design of a supercapacitor dictates the quality of energy being preserved in the device. Supercapacitors are connected in series for operation at higher potentials, can operate over a wide temperature range of -30 - 45 ˚C, and work for more than ten years.

With World market for wireless applications growing phenomenally, supercapacitors are used within portable appliances and powered by battery technology and thus to support the pulse requirements need to have high capacitance/capacity value capacitor products. Supercapacitors can supply a value of about 12mF with a leakage current varying from 55µA-130µA as against 2.2µF and 3µA for the Tantalum capacitor. They work at selected potential compared to tantalum capacitors that only apply 50% of the nominal potential. They respond well to high

discharge requirements for pulse applications, far more successfully than tantalum capacitors, which adversely suffer from degradation when subjected to constant high discharge and are comfortably stable when it comes to structure and electrical properties.

Intensive researches have been carried out on MnO_2-based electrode materials for adoption in pseudocapacitors owing to their high theoretical specific capacitance, good thermal and chemical stability, environmentally friendliness, availability and cost-effectiveness. Different methods have been adopted in synthesizing MnO_2-based electrode materials for the accomplishment of improved electrochemical performances of supercapacitors.

In this research, we have reported the synthesis of a metal oxide (MnO_2) structure that allows for a much higher contribution in pseudocapacitive response, via a novel reflux-hydrothermal technique. The adopted technique possesses a huge advantage for materials' morphological controls, thus resulting in enhanced electrochemical performances of the metal oxide electrodes. The as-synthesized materials comprise δ-MnO_2 as phase (*see Fig. 2*). The rose flower-like MnO_2 materials possess substantial pores, which are readily available to electrolyte ions. A high percentage of improvement was achieved by modifying the dwell time during the reflux-hydrothermal synthesis. The morphology, structure, adsorption-desorption, and electrochemical capability of the nanostructured materials were examined.

Neutral aqueous medium shows to be a fascinating electrolyte for ECs. Operational potential for the half cell in aqueous electrolyte could reach up to 0.8 V. Two different alkali metal sulphate salts solutions with the same concentrations (1 M) have been examined for this purpose, based on cost-effectiveness and ecological factors. Amongst these two electrolytes (1 M Li_2SO_4 and 1 M Na_2SO_4), 1 M Li_2SO_4 solution proved a better performance. A wide operational potential achieved for the material's half-cell is attributed to solvation ions, largely those for Li^+ and $SO4^{2-}$ ions. The substantial solvation energy of Li^+ and $SO4^{2-}$ ions, which is in the order of 160–

220 kJ/mol [30], is at the start of a high potential for water decomposition. A better charge propagation and higher specific capacitance value was observed for MnO_2-1H half-cell compared to the MnO_2-2H, MnO_2-4H and MnO_2-6H materials in 1 M Li_2SO_4 solution. A peak specific capacitance of ~ 387.1 F g^{-1} depending on active mass of the MnO_2 sample, alongside good rate capability and cycling stability were recorded for the sample with 1 h dwell time (MnO_2-1H) in difference to the other samples in 1 M Li_2SO_4. Excellent cycling stability of up to 5000 cycles performed at an applied specific current of 3 A g^{-1} was achieved for the three-electrode material.

2. EXPERIMENTAL DETAILS

2.1. Synthesis of the δ-MnO_2 samples

$KMnO_4$ (0.768 g) was first dissolved in 100 mL of deionized (DI) water, followed by drop-wise addition of HCl (32 %) upon magnetic stirring to give rise to a homogeneous mixture. The mixture was then refluxed upon continuous stirring (400 rpm) at a reaction temperature of 150 °C for a dwelling time of 1, 2, 4, and 6 h, separately. After cooling to room temperature, the supernatant was poured out and resulting solution was washed thoroughly with DI water until neutral. The resulting precipitate was dried overnight using electric oven in ambient condition at 60 °C. The recovered powdered samples were designated as MnO_2-1H, MnO_2-2H, MnO_2-4H, and MnO_2-6H according to their dwell time, respectively.

2.2. Characterization of the samples

Images of the as-prepared samples were acquired through the aid of a Zeiss Ultra Plus 55 field emission scanning electron microscope (FE-SEM) run at 1.0 kV. The structural analysis was performed by employing an XPERT-PRO X-ray diffractometer (PANalytical BV, Netherlands) with reflection geometry at 2θ values (5 – 90°) with a step size of 0.05°, working with a Cu $K\alpha$

radiation source (λ = 0.15418 nm) at 50 kV and 30 mA. N_2-absorption-desorption isotherms of the samples were achieved through the aid of a Micromeritics TriStar II 3020 device run at a relative pressure (P/P^o) ranging from 0.01–1.0 with the samples been pre-degassed at a temperature of 100 °C over a period of 16 h in vacuum before the analysis was performed. A Brunauer-Emmett-Teller (BET) and Barrett–Joyner–Halenda (BJH) model was adopted to estimate the samples' surface area and pore size distribution (PSD), respectively.

2.3. Electrochemical measurements

The three-electrode measurements of the as-prepared half-cells were done through the aid of a Bio-Logic VMP300 potentiostat (Knoxville TN, USA) utilizing the EC-Lab VI.41 software. The as-synthesized MnO_2 materials were prepared as working electrodes by muddling 80 % of the sample as working material with 10 % conductive carbon acetylene (CAB) along with 10 % of polyvinylidene (PVDF) adopted as binder in a few drops of 1-methyl 2-pyrollidone (NMP). The mixture was then stirred for ~ 120 min by using a magnetic stirrer at room temperature to form uniform slurry. The formed slurry was later pasted onto rectangular nickel foam with area and thickness of 1.0 x 1.0 cm^2 and 0.2 mm, respectively, serving as current collector. The as-prepared electrodes were subsequently dried overnight in an ambient oven at a temperature of 60 ^oC. The actual active material loading mass-per-area of the electrodes in the half-cells in various electrolytes was estimated to be ~ 4.0 mg cm^{-2}. All electrochemical measurements were done using 1 M Li_2SO_4 and 1 M Na_2SO_4 solutions, with the adoption of Ag/AgCl and glassy carbon as reference and counter electrodes, respectively. The fabricated electrodes were then explored by using cyclic voltammetry (CV), galvanostatic charge discharge (GCD) and electrochemical impedance spectroscopy (EIS), respectively.

The gravimetric specific capacitance, S_c of the half-cells was estimated in line with the equation stated below:

$$S_c = \frac{I_d \times \Delta t}{\Delta E} \quad (F\ g^{-1}) \tag{1}$$

Where I_d is specific current, which is applied current (A) per unit mass (g) of active material, and $\Delta E\ (= E_o - E_{IR-drop})$ is change in operating potential (V) for the single electrode. Δt is time (s) discharged by the electrode.

The single electrode*'s* coulombic efficiency, C_E was estimated over an electrode potential, E (V) by adopting the equation:

$$C_E = \frac{S_{cd}}{S_{cc}} \times 100\% \tag{2}$$

where $S_c$sc and $S_c$sd are the specific capacitance for charge and discharge processes, respectively.

3. RESULTS AND DISCUSSION

3.1. Morphological and structural evaluations

The SEM micrographs of the studied MnO_2 samples are as portrayed in Fig. 1. The figure (a-h) shows the samples' images at low and high magnifications, respectively. The SEM images confirmed the emergence of nanoflower constructed with intersected nano rose-like platelets morphologies (Fig. 1 (a-f), whose formation was brought about by the hydrothermal reflux process at the reaction temperature (150 ˚C). In Fig. 1 (g and h), a few nanorods appeared from the nanoflowers at 6 h, implying that a viable phase transition of the material occurred under the condition of reaction. The evolution of the few nanorods (Fig. 1 (g-h)) noticed for the MnO_2-6H sample is ascribed to the slow dissolution and recrystallization processes taking place alongside

with steady growth kinetic of nanorods at stable condition. The SEM images denote a robust interconnection between the reactions time and the yielded nanostructured samples.

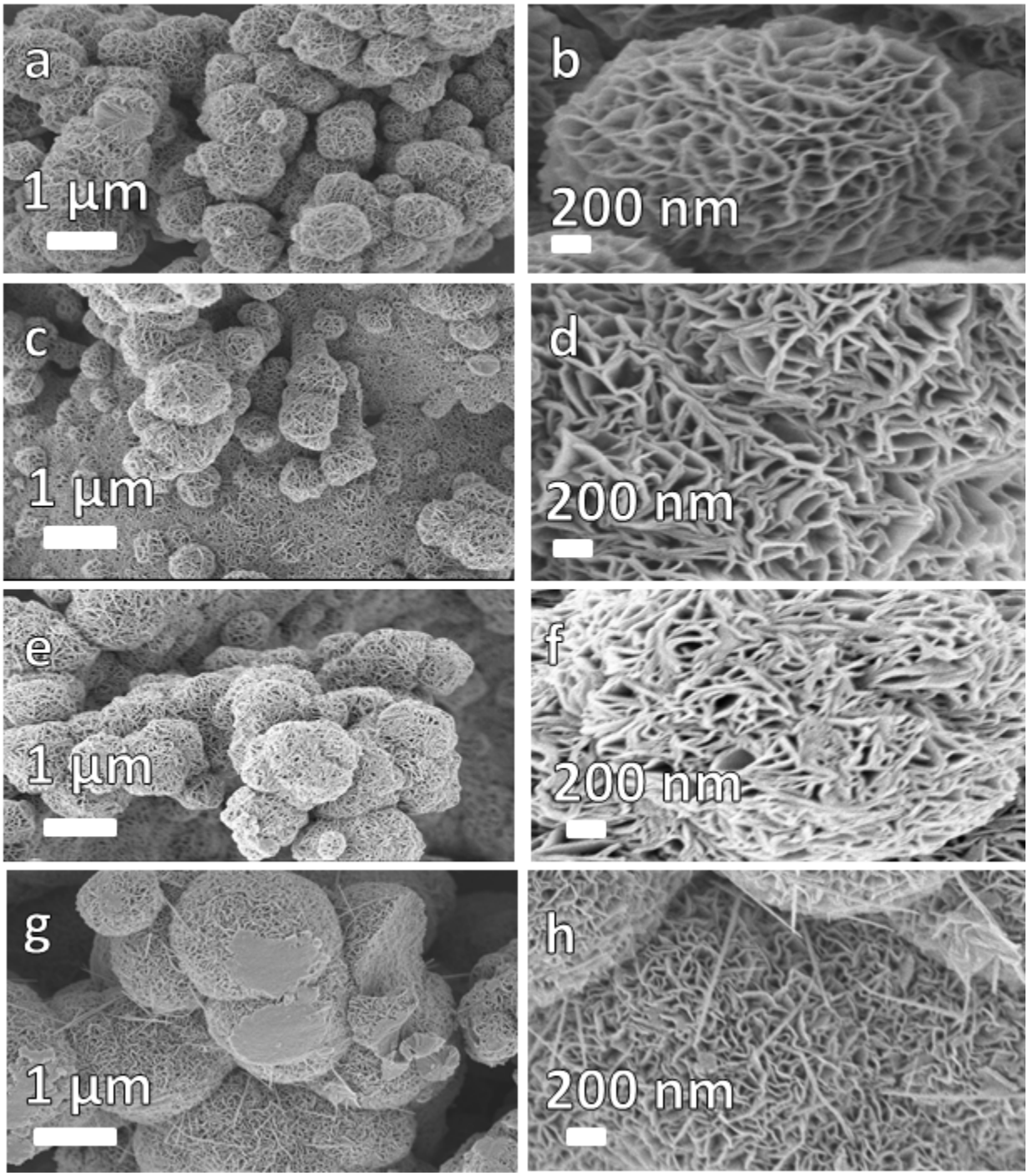

Fig. 1: SEM morphologies of (a-b) MnO_2-1H, (c-d) MnO_2-2H, (e-f) MnO_2-4H, and (g-h) MnO_2-6H at low and high magnifications, separately.

3.2. Formation mechanism of MnO_2 samples at various growth-time

Scheme 1 depicts a diagrammatic illustration of the formation of the various nano-whisker flower-like δ-MnO_2 materials. Scheme 1 (a) describes the formation of nano flower-like MnO_2 particles at 150 °C for 1 h dwell time of hydrothermal process, replicating the growth of nanostructured surfaces with distinct flower-like morphology. After a 2 h hydrothermal treatment as shown in Scheme 1 (b), an increase in size of individual nano flower-like particles was observed, showing wider loosened surfaces as compared to the 1 h dwelt time. At 4 h growth time (Scheme 1 (c)), most of MnO_2 nanoflowers are dispersed and tend to assemble [31]. The material's flower-like surfaces tend to collapse and become agglomerated. At subsequent increase in the hydrothermal dwelt time of 6 h as shown in Scheme 1 (d), the material's nano flower-like particles became more largely agglomerated with increased particle density and tend to loosen up thus lead to appearance of nanorods. As a result, the appearance of the rod-like architectures evolved through the nanoflower-like structures formed at the reflux-hydrothermal process temperature (150 ˚C). This nanorods appearance is attributed to the progressive dissolution and recrystallization processes alongside the low growth kinetic of nanorods at static condition [32].

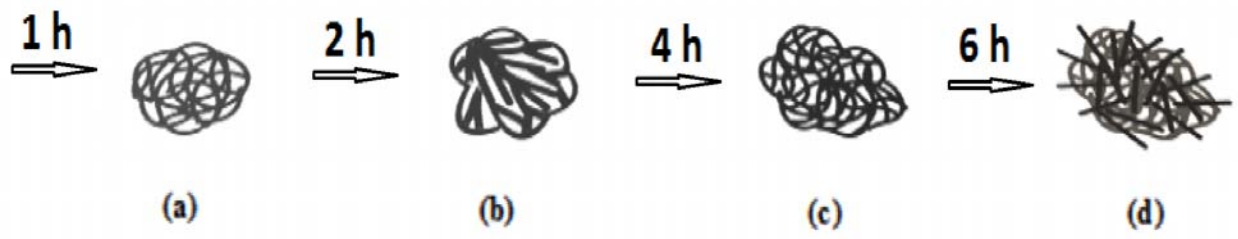

Scheme 1: Schematic diagrams of formation of the various MnO_2 samples prepared under the corresponding reflux-hydrothermal growth-time.

Fig. 2 depicts the XRD patterns for all the prepared MnO_2 samples at various reaction times. The XRD pattern is indexed in line with the monoclinic potassium birnessite according to the JCPDF No 43-1456 structure having the C2/m space group (Number: 12) with unit cell parameters in the order of a = 0.52 nm, b = 0.29 nm, c = 0.73 nm, and β is ~ 103.18° [33,34]. As observed in the Figure, the (0 0 1) and (0 0 2) planes corresponding to about 2θ equals to ~ 12.4 and 24.8˚ are representative of the birnessite phase layered δ-MnO_2. The noticed (1 0 0) plane is an indication of crystallized water alongside formation of water-to-MnO_2 interlayer [33,35,36]. Besides, the peak implies a mixture of amorphous and nanocrystalline nature of the materials due to the nanoflower-like architecture of the as-prepared δ-MnO_2 materials. An increase in crystallinity exhibited by appearance of sharper peaks with respect to increase of reaction time is observed from 1 h to 4 h, but with a less sharp peak for the MnO_2-6H sample, which was prepared for 6 h.

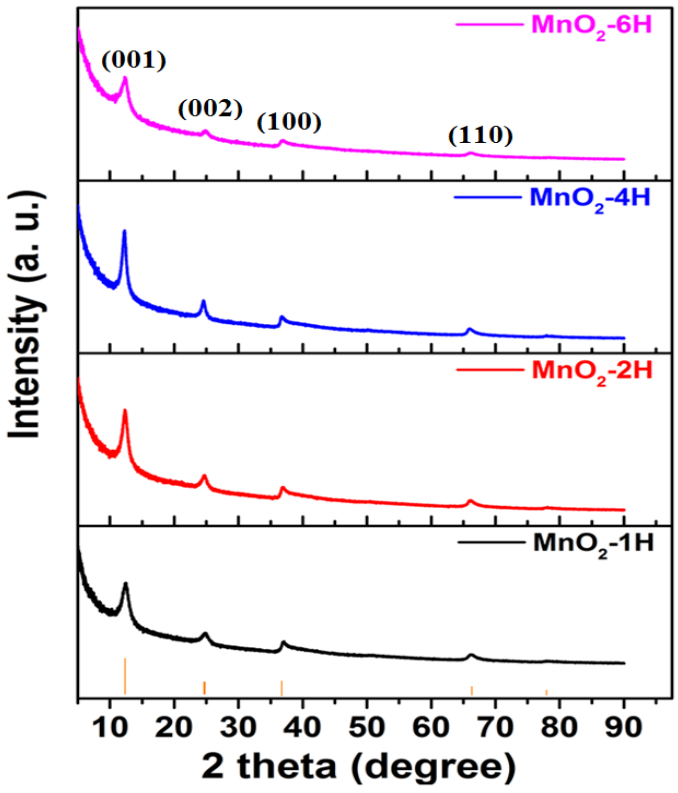

Fig. 2: XRD spectrum of (a) MnO_2-1H, (b) MnO_2-2H, (c) MnO_2-4H and (d) MnO_2-6H, respectively.

Fig. 3 (a-b) reveals a nitrogen adsorption/desorption isotherm along with its pore size distribution (PSD) curves for the various MnO_2 samples adopted as electrode materials. The observed pattern of the isotherm and PSD demonstrated the rather microporous nature of the samples; yet, the remarkable existence of mesopores cannot be disregarded, most especially for the MnO_2-1H sample. From Fig. 3(a), all samples reveal a type-III characteristic, alongside H3-type hysteresis, depicting materials consisting of non-rigid aggregates of plate-like particles or assemblages of slit-shaped pores [37]. The PSD plots are shown in Fig. 3(b), confirming the presence of micropores and mesopores in the samples' structures (except for MnO_2-4H, which is majorly of micropores) as earlier observed from the isotherms revealed in Fig. 3(a). Both the micropores and mesopores play a crucial part in charge agglomeration. The micropores account for charge storage and ion adsorption, while the mesopores serve as channels for ions through transport from bulk of electrolyte to the interface between the electrode and electrolyte [30]. On the basis of this, the electrolyte ions should ideally compliment the pore sizes of the electrode material to attain convincing results of charge propagation and avoid some steric restraints [30]. In consequence, we have provided a detailed modelling of the electrolyte ions achieved by the aid of a FreeCAD Autodesk Meshmixer 3.5 3D software as presented in Scheme 2, which shows shapes of the ions. Table 1 shows the dimensions of the alkali metals cations and sulphate anion in both the 1 M Li_2SO_4 and Na_2SO_4 aqueous solutions. The estimated values *(see Table 1*) for both the sulphate anion and the alkali metals' (Li^+ and Na^+) cations agree well with the literature [30,38,39]. Some other physical properties of the ions such as diffusion coefficients, solvation energies, mobilities together with ion–to-ion, ion–to-solvent along with solvent–to-solvent interactions might be determining factors considering the electrochemical performances. These properties directly influence not only the convincing values of capacitance but as well, the

superior charge propagation, leakage currents as well as the feasibility of extending operational potential range.

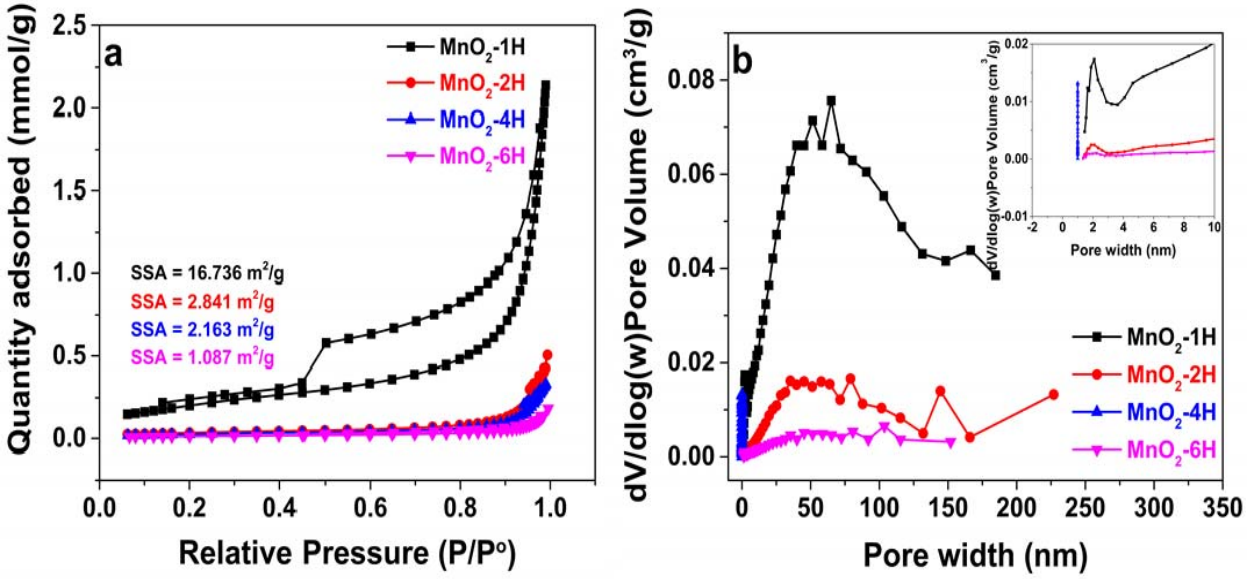

Fig. 3: (a) N_2 physisorption isotherms and (b) equivalent pore size distribution of the MnO_2 samples grown at different temperatures.

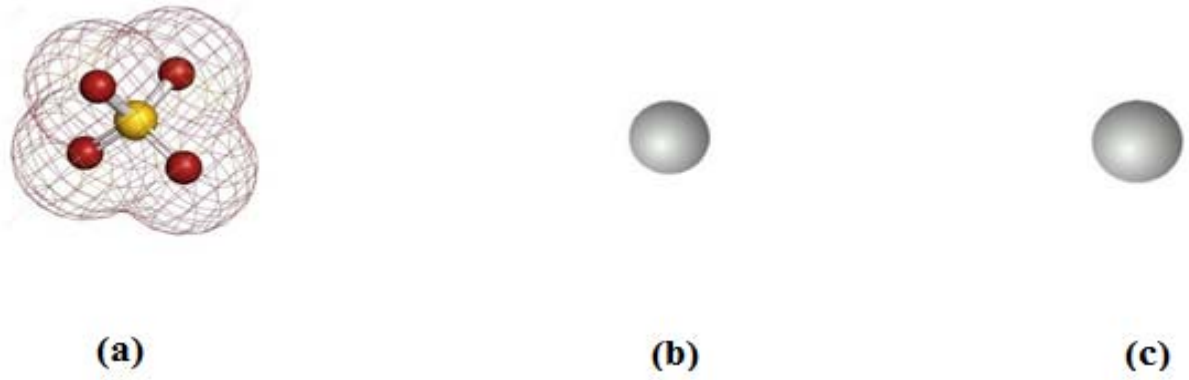

Scheme 2: Shape and dimensions of ion in aqueous electrolytes (a) sulphate anion (SO_4^{2-}) with surrounding mesh denoting its molecular orbitals, (b) lithium cation (Li^+) and (c) sodium cation (Na^+), respectively. Note: The scale amongst presented pictures in scheme 2 is not preserved.

Table 1: Estimated dimensions of the lithium and sodium cations, and sulphate anion in both 1 M Li_2SO_4 and Na_2SO_4 aqueous solutions adopted in this work.

Ion	**SO_4^{2-}**	**Li^+**	**Na^+**
Hydrated	0.73 nm	0.38 nm	0.36 nm

3.3. Electrochemical analysis

3.3.1. Electrochemical analysis of half-cell electrodes

To examine the electrochemical properties of the various MnO_2 samples, a three-electrode configuration was adopted, which was performed using both 1 M Li_2SO_4 and 1 M Na_2SO_4 as investigation electrolytes. Fig. 4 (a and c) depicts and compares the associated CV profiles taken at a scan rate of 20 mV s^{-1} measured from 0.0 V to 0.8 V operating potential for the various MnO_2 samples in this work by employing 1 M Li_2SO_4 and 1 M Na_2SO_4 solutions, respectively. From the figure, the material synthesized at a dwelt time of 1 h displayed a better performance in terms of output currents as compared to the other samples. The displayed higher current response for the MnO_2-1H indicates a higher specific capacitance against the other samples as demonstrated in Fig. 4 (a and c). Fig. 4 (b and d) reveals a comparison of the GCD profiles for the samples performed at 0.5 A g^{-1} using 1 M Li_2SO_4 and 1 M Na_2SO_4, individually. The observed GCD profiles (like the CV profiles in Fig. 4 (a and c)) show a typical of pseudocapacitive properties, which is expected of a material like the MnO_2. At the low specific current (0.5 A g^{-1}), the observed quite resistive character of the GCD profiles as depicted in Fig. 4 (d) suggests some difficulties in charge propagation, leading to the very low coulombic efficiency recorded for the materials. This behaviour is attributed to Faradaic decomposition reactions occurring as maximum potential, E_{max} is approached. At E_{max} (0.8 V), Faradaic hydrogen electrosorption occurs alongside electric double-layer charging thus, induces non-symmetry of the GCD profiles. In comparison to the other samples, the MnO_2-1H electrode

produced a longer discharge time for both the electrolytes, which means it has much higher specific capacitance than other samples as was noticed in the case of CV measurements in Fig. 4 (a and c). This is strictly ascribed to the sample's higher specific surface area as well as pore size distributions, which could be important in providing elevated adsorbate accessibility alongside larger flow paths to pores thus, enhancing storage of charges [37]. The observed results show the double-edged influence of high surface area in the electrode performance, leading to more active sites especially during charging-discharging contributing higher specific capacitance [40,41]. The electrochemical impedance spectroscopy (EIS) was adopted to further analyze the samples' electrochemical performances. Fig. 5 (a and b) is a representation of Nyquist plot of the various samples estimated at a potential of 0.0 V and within a frequency ranging from 10 mHz – 100 kHz. The observed semi-circle in the high-frequency region for the MnO_2-1H sample in Fig. 5(a) and for all the samples in Fig. 5(b) is attributed to some resistances due to electron transfer from the electrode through the electrolyte. Nevertheless, the MnO_2-1H sample still displays a shorter diffusion path length (see the inset to Fig. 5(a and b)) and nearer to the ideal vertical line as compared to the other samples. This suggests that the electrode is more electrochemically conductive than MnO_2-2H, MnO_2-4H, and MnO_2-6H electrodes. Moreover, the Nyquist plots for MnO_2 electrodes were fitted in line with the corresponding circuits as shown in Fig. 5 (ai and bi), respectively, by employing a ZFIT/EC-Lab version 11.02 software. In the circuits, the R_S is connected in series with two branches, namely, the constant phase element Q, which is connected in parallel with the charge transfer resistance, R_1. The transition from high-low frequency region is modelled by Warburg diffusion element and denoted by W that is in series with R_1. The second and third branch (Fig. b(i)), respectively, composed of another constant phase element Q, which is connected in parallel with single resistance. These second and third branches denote the middle and low frequency region, respectively. Fig. 5 (c) demonstrates a

comparison of specific capacitances for the various electrodes measured at 0.5 A g^{-1} in both solutions. The MnO_2-1H proved a superior value of ~ 387.1 and 222.5 F g^{-1} compared to 230.6 and 201.5 F g^{-1}, 242.5 and 202.5 F g^{-1}, and 193.1 and 113.7 F g^{-1} for MnO_2-2H, MnO_2-4H, and MnO_2-6H electrodes in 1 M Li_2SO_4 and 1 M Na_2SO_4, separately.

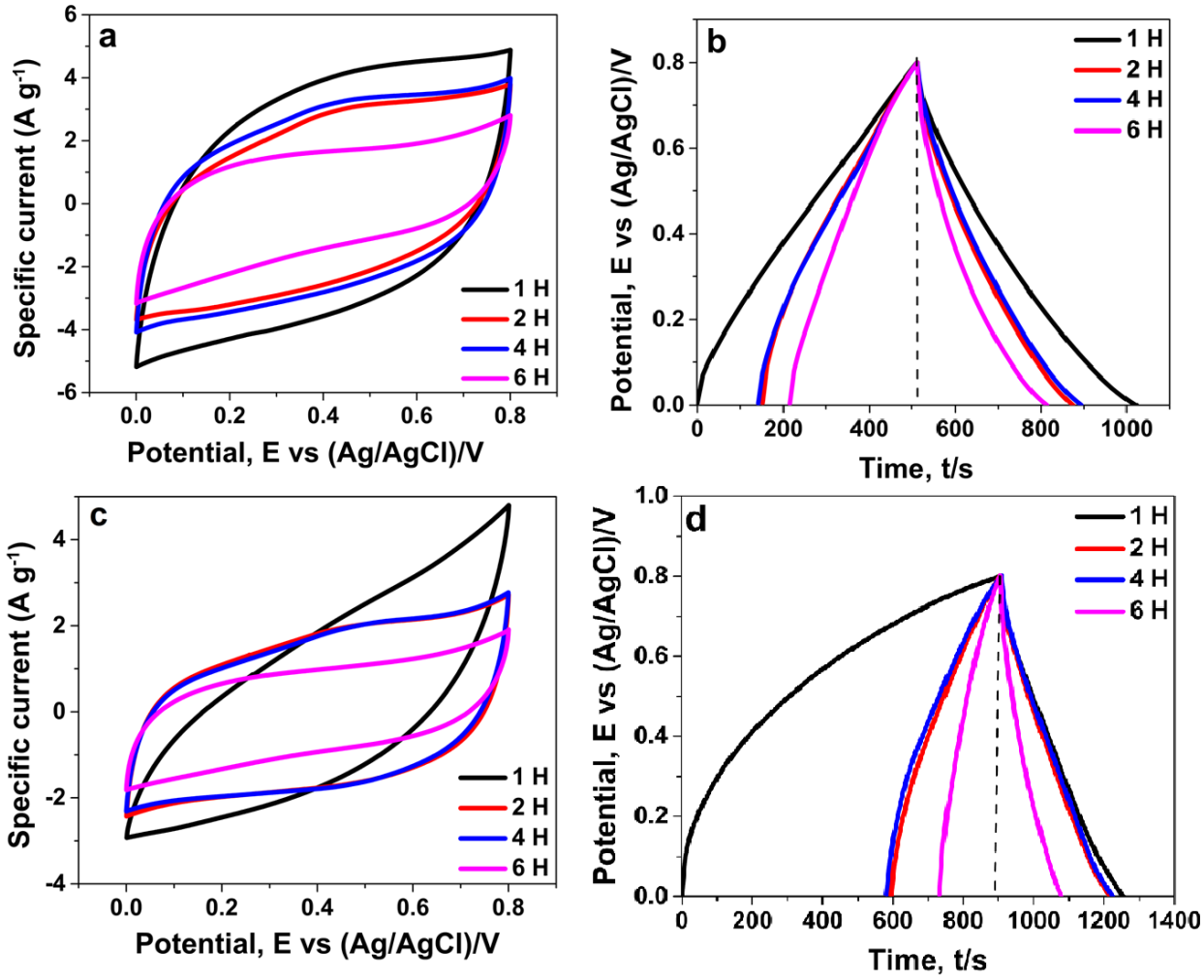

Fig. 4: (a) CV profiles, and (b) GCD profiles measured in 1 M Li_2SO_4 at a scan rates of 20 mV s^{-1} and a specific current of 0.5 A g^{-1}, respectively, (c) CV profiles, and (d) GCD profiles measured in 1 M Na_2SO_4 at a scan rates of 20 mV s^{-1} and a specific current of 0.5 A g^{-1}, respectively, for the MnO_2 electrodes.

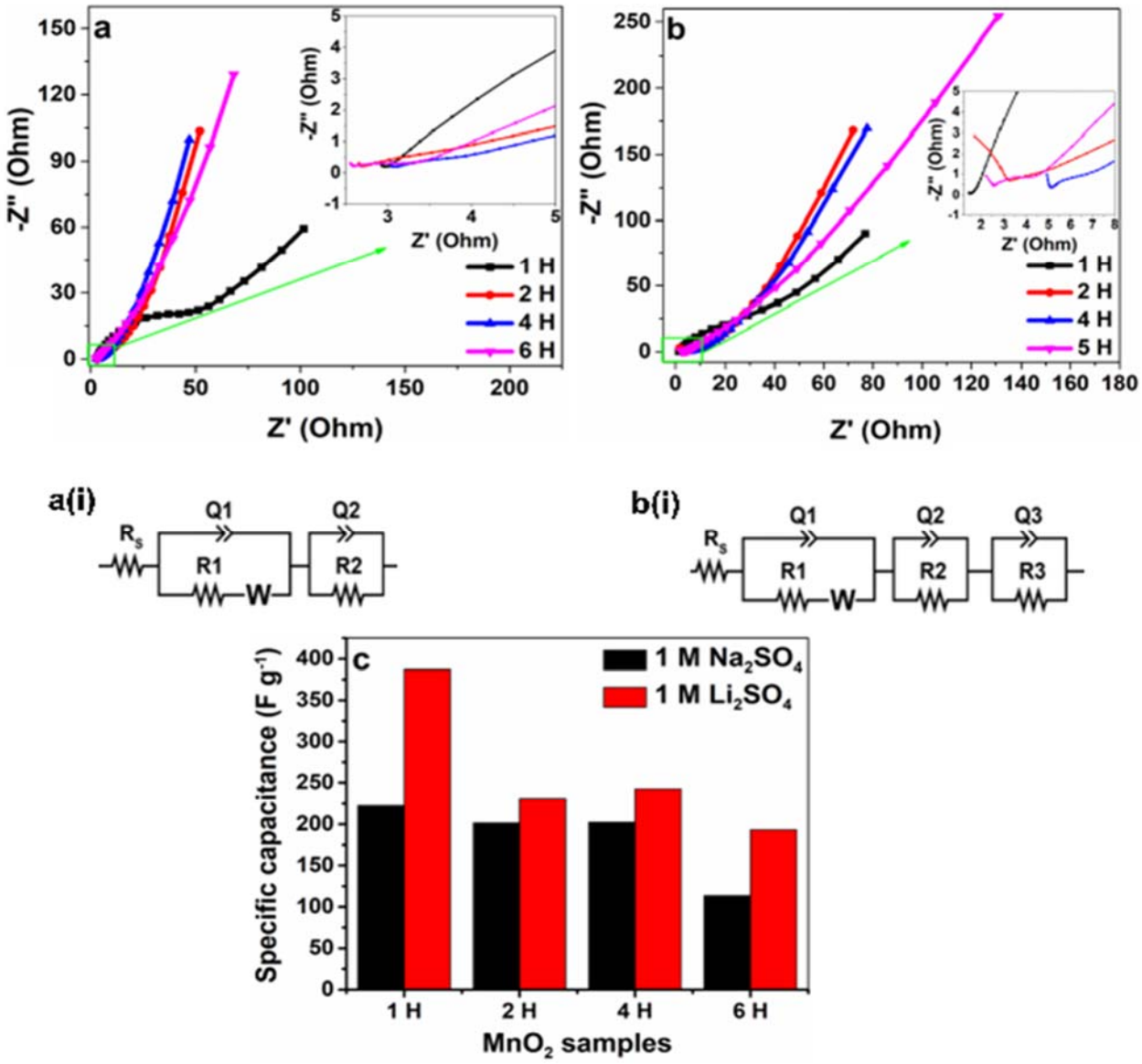

Fig. 5: Nyquist impedance plots of the various MnO_2 samples (a) in 1 M Li_2SO_4 and (b) in 1 M Na_2SO_4 solutions, and their fitting equivalent circuits as (ai) and (bi), respectively, and (c) comparison of specific capacitance values taken at a specific current of 0.5 a g^{-1} for the samples in both 1 M Li_2SO_4 and 1 M Na_2SO_4 solutions.

Fig. 6(a-b) depicts the relationship between CV and GCD profiles of the MnO_2-1H sample in the two solutions at a sweep rate of 20 mV s^{-1} and specific current of 0.5 A g^{-1} in a working potential ranging from 0.0–0.8 V, respectively. The 1 M Li_2SO_4 exhibits a higher current response (Fig. 6(a)) as well as longer discharge time as demonstrated in Fig. 6(b) for the electrode, showing the efficacy of the material

in the electrolyte.

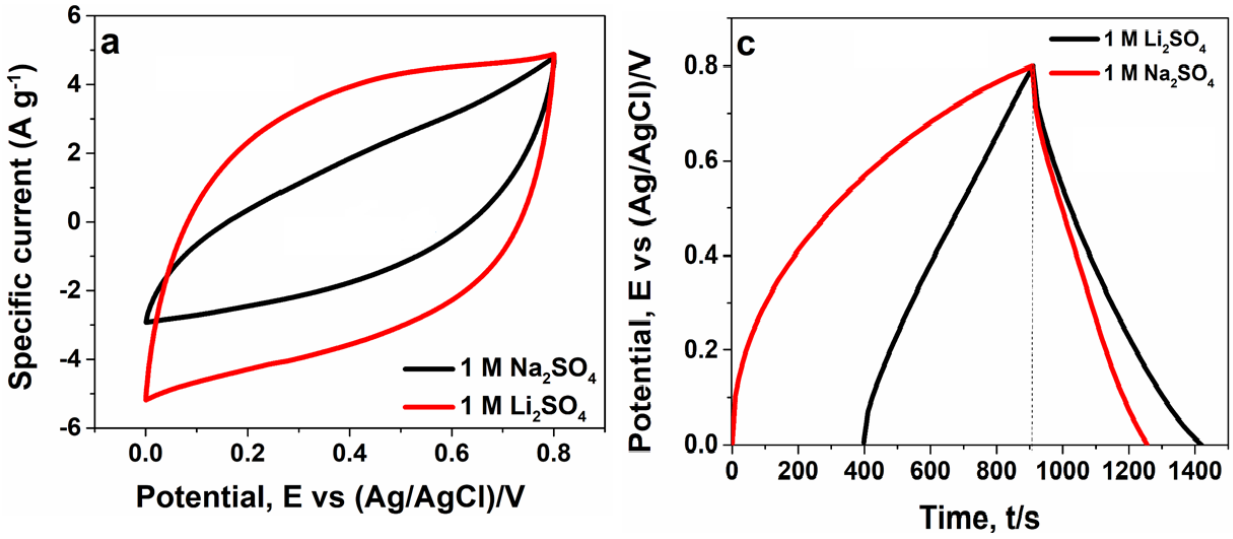

Fig. 6: (a) CV and (b) CD profiles of MnO_2-1H at a sweep rate of 20 mV s^{-1} and specific current of 0.5 A g^{-1} in both 1 M Li_2SO_4 and 1 M Na_2SO_4 solutions, respectively.

From Fig. 6, it is observed that the 1 M Li_2SO_4 solution gives a better charge propagation, which correlate well with satisfying values of specific capacitance produced by the electrolyte as demonstrated in Fig. 5c. This is attributed to the Li^+ mobilities compared to its Na^+ counterpart. The size of these alkali metal ions increases in the order as stated below:

order: $Na^+ > Li^+$.

Generally, smaller ions possess higher conductivity than the larger ions owing to their small areas, which provide less resistance as they move via the electrolyte solution. The degree of hydration of the two alkali metals ions increases as:

$Li^+ > Na^+$.

The smaller Li^+ is considered to have a higher charge density than the Na^+, which gives it a large hydration shell that moves with it in aqueous solutions. Thus, the lithium ions slightly lower conductivities than that of sodium ions in aqueous solutions.

Though, the two metal ions are highly hydrated, the smaller the size of the ion, the greater is the degree of its hydration. Therefore, Li^+ becomes much more hydrated than the Na^+. Due to the larger degree of hydration of the Li^+, its ionic effective size is greater than that of Na^+. This accounts for swift ions transfer into the electrode-electrolyte interface required by the pseudocapacitive material for fast redox processes, which therefore enhances the mobility and efficient charge propagation in the well-saturated porous structure of the electrode.

Fig. 7 displays the various CV profiles obtained for the sample synthesized for 1 h (MnO_2-1H) measured at distint scan rates in both Li_2SO_4 and Na_2SO_4 solutions. Fig. 7 (a) reveals the CV profile at 5 mV s^{-1}. The comparatively slow scan rate could reveal a significant difference in charge propagation for the sample in 1 M Li_2SO_4 over the 1 M Na_2SO_4 electrolytes. For a moderate sweep rate of 10 mV s^{-1} (see Fig. 7 (b)), the Li_2SO_4 solution still seems to be more promising than the Na_2SO_4 electrolyte, taking into account the charge propagation. For a fast rate of 20, 40, and 50 mV s^{--1} as depicted in Fig. 7 (c, d and e), respectively, the electrode shows a comparatively resistive behaviour of the voltammograms in both solutions, which demonstrates some difficulties in charge propagation. Nevertheless, the1 M Li_2SO_4 still proved a better performance over the 1 M Na_2SO_4 Solution. Fig. 7 (f) compares the variation of coulombic efficiency against cycle number for the MnO_2-1H electrode in both 1 M Li_2SO_4 and 1 M Na_2SO_4. The result indicates an efficiency of ~ 100 % in 1 M Li_2SO_4 as against 98 % in 1 M Na_2SO_4.

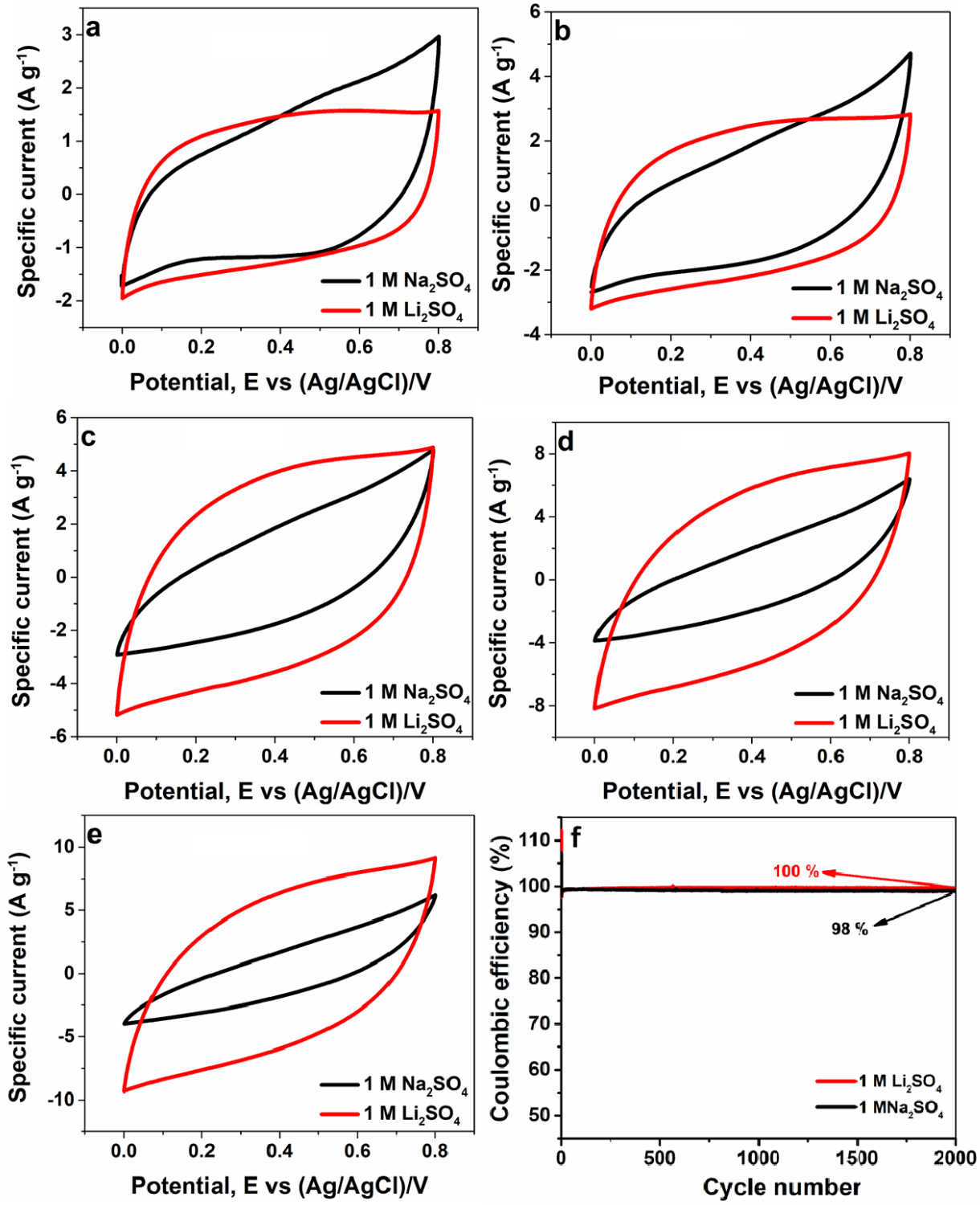

Fig. 7: CV curves at distinct sweep rate of (a) 5, (b) 10, (c) 20, (d) 40, (e) 50 mV s^{-1}, and (f) Coulombic efficiency versus cycle number measured at 3 A g^{-1} for the MnO_2-1H in 1 M Li_2SO_4 and 1 M Na_2SO_4 solutions, respectively.

To better examine the electrochemical properties of MnO_2-1H material in 1 M Li_2SO_4 solution, the CV and GCD of the single electrode were estimated at distinct sweep rates and specific currents, separately. Fig. 8(a) reveals the associated CV profiles of the material at an operating potential range of 0.0–0.8 V. Correspondingly, Fig. 8(b) expresses the GCD profiles of the material at distinct specific currents in a potential window ranging from 0.0–0.8 V. The variation of specific capacitances against the specific currents estimated according to equation 1 is as expressed in Fig. 8(c). The electrode proved a maximum specific capacitance of ~ 387.1 F g^{-1} at a specific current of 0.5 a g^{-1}, and could even yield a specific capacitance of 132.7 F g^{-1} at a very high specific current of 20 A g^{-1}. The observed specific capacitance decrease with respect to increase in specific current is ascribed to the ion exchange mechanism. In this regard, at a low specific current, the SO_4^{2-} has got sufficient time to link up with the electrode's surface, which will be diffused in and out of the electrode during charge and discharge operations. Thus, a high specific capacitance is achieved. Nonetheless, at the higher specific currents, less charge is transferred at the electrode-electrolyte surface resulting in low specific capacitance.

The values of specific capacitance proved by the MnO_2 electrodes in this work as displayed in figures 5 (c) and 8 (c), respectively, revealed considerable enhancement when compared to other similar birnessite phase manganese oxide material electrodes in aqueous solutions. Such materials as presented in Table 2.

Table 2: Electrochemical performances of similar birnessite phase manganese oxide electrodes extracted from the literature.

Electrode	Specific capacitance (F g^{-1})	Electrolyte	Specific current/Scan rate	Reference
Transformed birnessite MnO_2	251.4	1 M Na_2SO_4	1 A g^{-1}	[42]
Flower shaped δ-MnO_2	174.8; 256.5	1 M LiOH; Na_2SO_4	0.3 A g^{-1}	[35]
Fragmented platelets MnO_2 Birnessite	225	0.5 M K_2SO_4	5 mV s^{-1}	[33]
MnO2 birnessite structure electrode	145	0.5 M Na_2SO_4	2 mV s^{-1}	[34]
Microwave–hydrothermally synthesized birnessite-type MnO_2 nanospheres	210	1 M Na_2SO_4	200 mA g^{-1}	[43]
Interwoven ultrathin birnessite-type MnO_2 nanosheets,	365	1 M Na_2SO_4	0.25 A g^{-1}	[44]
Birnessite MnO_2-decorated hollow dandelion-like CuO	228	1 M Na_2SO_4	0.25 A g^{-1}	[45]
Birnessite-type MnO_2 as positive electrode	76.8	2.5 M KNO_3	2 A g^{-1}	[46]
Reflux-hydrothermal synthesized nanoflower-like birnessite MnO_2	387.1; 222.5	1 M LiOH; 1 M Na_2SO_4	0.5 A g^{-1}	This work

The chosen papers in Table 1 are of special interest owing to their remarkable electrochemical performances, which include as wider potential window, higher specific capacitance and significant cycle stability.

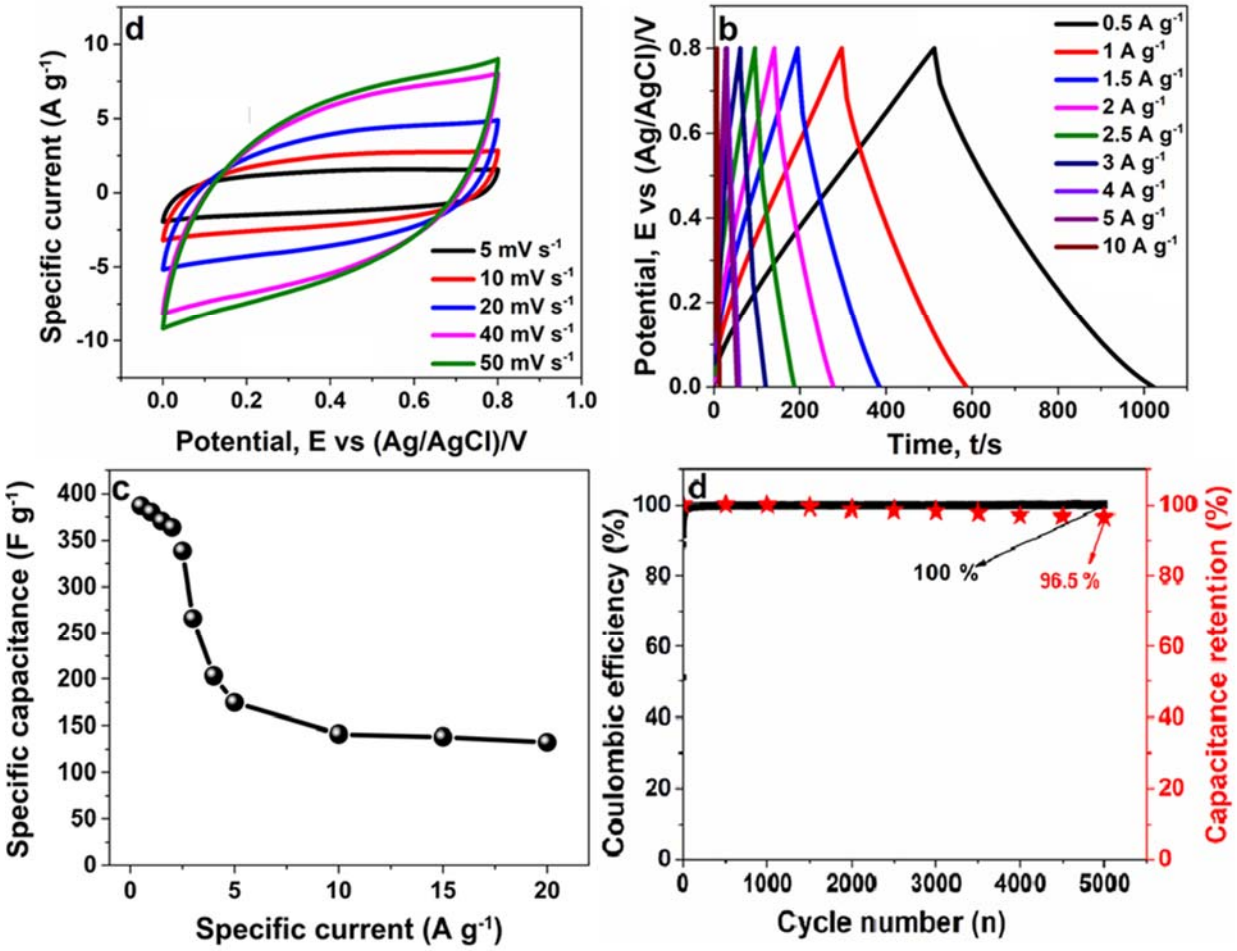

Fig. 8: (a) CV and (b) CD profiles at various scan rates and specific currents, (c) variation of specific capacitance against specific currents, and (d) variations of coulombic efficiency and capacitance retention of MnO_2-1H electrode against the cycle number evaluated at 3 A g^{-1} in 1 M Li_2SO_4 solution, respectively.

The MnO_2-1H was further cycled over a prolonged cycling test of 5000 cycles to further ascertain its stability. The result of which is demonstrated in Fig. 8 (d). From the figure, it is noticed that the electrode proves a remarkable coulombic efficiency of 100 % and could as well preserve about 96.5 % of its inceptive capacitance after a cycling test conducted for over 5000 cycles at a specific current density of 3 A g^{-1}. This impressive behaviour is attributed to the material's mesoporous structure, which could play a significant contribution in enhancing the effectual electrode surface area, and enabling solution permeation, which in turn shortenss the

electron pathway in the active materials [47,48]. The sample's structure is well available for the reactant molecules and Li^+ through the interlayer space. Besides, this structure could result in effective ion and electron transfer, restricting the electrode's volumetric reordering during charge and discharge processes [47,49]. Fig. 9 (a and b) shows the MnO_2-1H electrode's SEM morphology and EIS plot taken after the cycling test of over 5000 cycles. The material reveals no significant change in morphology (as compared to the image in Fig. 1 (a)) and electrical properties even after the long-term cycling. This indicates the electrode's superior structural and electrochemical stability as compared to the other samples.

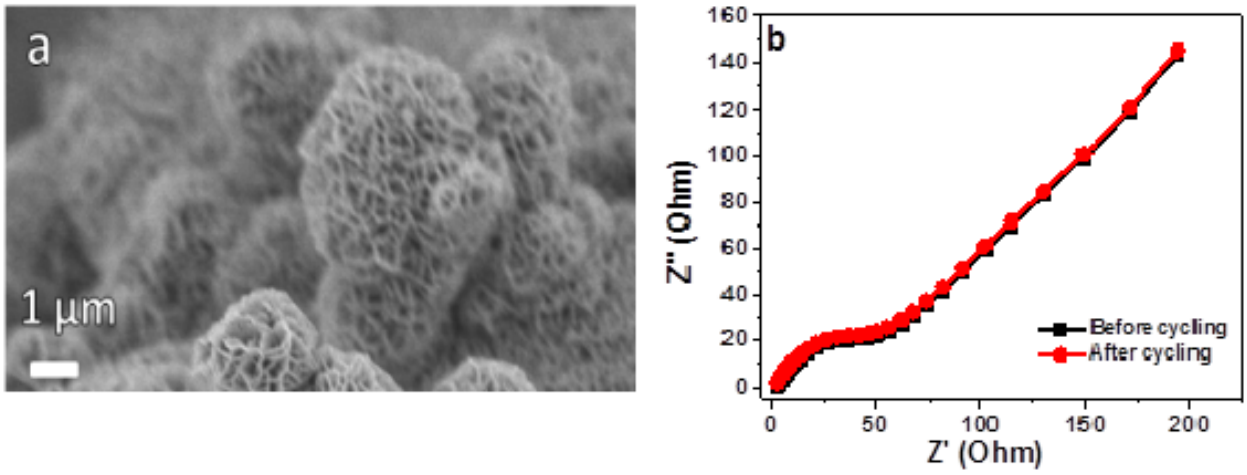

Fig. 9: (a) SEM image and (b) EIS Nyquist plot of MnO_2-1H electrode after the 5000 cycles cycling test at 3 A g^{-1} in 1 M Li_2SO_4 solution, respectively.

4. CONCLUSION

Neutral 1 M Li_2SO_4, and 1 M Na_2SO_4 have been examined as potential liquid media for MnO_2 materials synthesized at different reaction times as electrodes for supercapacitors application. The 1 M Li_2SO_4 solution was more promising in terms of higher values of specific capacitance, faster charge propagation, alongside better cycling stability for over a 5000-cycling test compared to the Na_2SO_4 electrolyte. A specific capacitance of ~ 387.1 F g^{-1} was recorded for the

MnO_2-1H compared to 230.6, 242.5 and 193.1 F g^{-1} for MnO_2-2H, MnO_2-4H and MnO_2-6H, respectively, at a specific current of 0.5 A g^{-1} using 1 M Li_2SO_4. Interestingly, the MnO_2-1H electrode could prove a value of 132.7 F g^{-1} even at a high discharging specific current of 20 A g^{-1}, indicating the materials swift charge transfer capability as compared to the other materials. On the contrary, more reaction times like 2H, 4H, and 6H in both 1 M Li_2SO_4 and 1 M Na_2SO_4 electrolytes resulted in slightly lower values of capacitance, though the charge propagation of the materials utilizing the two solutions is somewhat satisfactory, which is ascribed to the spatial relationships of atoms in the samples' solvated molecules. Thus, intensifying rapid charge transfer in the pores of the materials.

ACKNOWLEDGEMENTS

We sincerely acknowledge research support from South African Research Chairs Initiative of the Department of Science and Technology and National Research Foundation (NRF) of South Africa (Grant No. 61056). K. O. Oyedotun acknowledges financial support from the University of Pretoria and the NRF, South Africa.

REFERENCES

[1] P. Simon, Y. Gogotsi, Materials for electrochemical capacitors, 7 (2008) 1–10. doi:10.1038/nmat2297.

[2] J.P. Holdren, Energy and sustainability, Science (80-.). 315 (2007) 737. doi:10.1126/science.1139792.

[3] D. Ginley, M.A. Green, R. Collins, Solar energy conversion toward 1 terawatt, MRS Bull. 33 (2008) 355–364. doi:10.1557/mrs2008.71.

[4] V.S. Arunachalam, E.L. Fleischer, The Global Energy Landscape and Materials

Innovation, MRS Bull. 33 (2008) 264–288. doi:10.1557/mrs2008.61.

[5] H. Wang, H. Dai, Strongly coupled inorganic–nano-carbon hybrid materials for energy storage, Chem. Soc. Rev. 42 (2013) 3088–3113. doi:10.1039/c2cs35307e.

[6] G. Yu, X. Xie, L. Pan, Z. Bao, Y. Cui, Hybrid nanostructured materials for high-performance electrochemical capacitors, Nano Energy. 2 (2013) 213–234. doi:10.1016/j.nanoen.2012.10.006.

[7] A.S. Aricò, P. Bruce, B. Scrosati, J.-M. Tarascon, W. van Schalkwijk, Nanostructured materials for advanced energy conversion and storage devices, Nat. Mater. 4 (2005) 366–377. doi:10.1038/nmat1368.

[8] B. Dunn, H. Kamath, J.M. Tarascon, Electrical energy storage for the grid: A battery of choices, Science (80-.). 334 (2011) 928–935. doi:10.1126/science.1212741.

[9] A. Manthiram, A. Vadivel Murugan, A. Sarkar, T. Muraliganth, Nanostructured electrode materials for electrochemical energy storage and conversion, Energy Environ. Sci. 1 (2008) 621–638. doi:10.1039/b811802g.

[10] K.O. Oyedotun, T.M. Masikhwa, S. Lindberg, A. Matic, P. Johansson, N. Manyala, Comparison of ionic liquid electrolyte to aqueous electrolytes on carbon nanofibres supercapacitor electrode derived from oxygen-functionalized graphene, Chem. Eng. J. 375 (2019) 121906. doi:10.1016/j.cej.2019.121906.

[11] S. Liu, Y. Yin, K.S. Hui, K.N. Hui, S.C. Lee, S.C. Jun, High-Performance Flexible Quasi-Solid-State Supercapacitors Realized by Molybdenum Dioxide@Nitrogen-Doped Carbon and Copper Cobalt Sulfide Tubular Nanostructures, Adv. Sci. 5 (2018) 1800733. doi:10.1002/advs.201800733.

[12] S. Liu, K.S. Hui, K.N. Hui, 1 D Hierarchical MnCo2O4 Nanowire@MnO2 Sheet Core–Shell Arrays on Graphite Paper as Superior Electrodes for Asymmetric Supercapacitors, ChemNanoMat. 1 (2015) 593–602. doi:10.1002/cnma.201500105.

[13] S. Wu, K.S. Hui, K.N. Hui, Carbon nanotube@manganese oxide nanosheet core-shell structure encapsulated within reduced graphene oxide film for flexible all-solid-state asymmetric supercapacitors, Carbon N. Y. 132 (2018) 776–784.

doi:10.1016/j.carbon.2017.12.051.

[14] W. Xu, B. Mu, W. Zhang, A. Wang, Facile hydrothermal synthesis of tubular kapok fiber/MnO2 composites and application in supercapacitors, RSC Adv. 5 (2015) 64065–64075. doi:10.1039/c5ra13602d.

[15] S. Liu, Y. Yin, D. Ni, K.S. Hui, K.N. Hui, S. Lee, C.Y. Ouyang, S.C. Jun, Phosphorous-containing oxygen-deficient cobalt molybdate as an advanced electrode material for supercapacitors, Energy Storage Mater. 19 (2019) 186–196. doi:10.1016/j.ensm.2018.10.022.

[16] K.O. Oyedotun, N. Manyala, Graphene foam–based electrochemical capacitors, Curr. Opin. Electrochem. 21 (2020) 125–131. doi:10.1016/j.coelec.2019.12.010.

[17] S. Wu, K.S. Hui, K.N. Hui, K.H. Kim, Ultrathin porous NiO nanoflake arrays on nickel foam as an advanced electrode for high performance asymmetric supercapacitors, J. Mater. Chem. A. 4 (2016) 9113–9123. doi:10.1039/c6ta02005d.

[18] B.Y. Guan, L. Yu, X. Wang, S. Song, X.W.D. Lou, Formation of Onion-Like NiCo2S4 Particles via Sequential Ion-Exchange for Hybrid Supercapacitors, Adv. Mater. 29 (2017) 1605051. doi:10.1002/adma.201605051.

[19] J. Jiang, A. Kucernak, Electrochemical supercapacitor material based on manganese oxide: Preparation and characterization, Electrochim. Acta. 47 (2002) 2381–2386. doi:10.1016/S0013-4686(02)00031-2.

[20] H. Ma, J. He, D.B. Xiong, J. Wu, Q. Li, V. Dravid, Y. Zhao, Nickel Cobalt Hydroxide @Reduced Graphene Oxide Hybrid Nanolayers for High Performance Asymmetric Supercapacitors with Remarkable Cycling Stability, ACS Appl. Mater. Interfaces. 8 (2016) 1992–2000. doi:10.1021/acsami.5b10280.

[21] S.G. Kandalkar, J.L. Gunjakar, C.D. Lokhande, Preparation of cobalt oxide thin films and its use in supercapacitor application, Appl. Surf. Sci. 254 (2008) 5540–5544. doi:10.1016/j.apsusc.2008.02.163.

[22] A.A. Mirghni, K.O. Oyedotun, O. Olaniyan, B.A. Mahmoud, N.F. Sylla, N. Manyala, Electrochemical analysis of Na-Ni bimetallic phosphate electrodes for supercapacitor

applications, RSC Adv. 9 (2019) 25012–25021. doi:10.1039/c9ra04487f.

[23] C.C. Hu, K.H. Chang, M.C. Lin, Y.T. Wu, Design and tailoring of the nanotubular arrayed architecture of hydrous RuO2 for next generation supercapacitors, Nano Lett. 6 (2006) 2690–2695. doi:10.1021/nl061576a.

[24] Z.J. Han, S. Pineda, A.T. Murdock, D.H. Seo, K. (Ken) Ostrikov, A. Bendavid, RuO2-coated vertical graphene hybrid electrodes for high-performance solid-state supercapacitors, J. Mater. Chem. A. 5 (2017) 17293–17301. doi:10.1039/c7ta03355a.

[25] W. Xu, Z. Jiang, Q. Yang, W. Huo, M.S. Javed, Y. Li, L. Huang, X. Gu, C. Hu, Approaching the lithium-manganese oxides' energy storage limit with Li2MnO3 nanorods for high-performance supercapacitor, Nano Energy. 43 (2018) 168–176. doi:10.1016/j.nanoen.2017.10.046.

[26] S. Lian, C. Sun, W. Xu, W. Huo, Y. Luo, K. Zhao, G. Yao, W. Xu, Y. Zhang, Z. Li, K. Yu, H. Zhao, H. Cheng, J. Zhang, L. Mai, Built-in oriented electric field facilitating durable Zn[sbnd]MnO2 battery, Nano Energy. 62 (2019) 79–84. doi:10.1016/j.nanoen.2019.04.038.

[27] K. Zhao, C. Sun, Y. Yu, Y. Dong, C. Zhang, C. Wang, P.M. Voyles, L. Mai, X. Wang, Surface Gradient Ti-Doped MnO 2 Nanowires for High-Rate and Long-Life Lithium Battery, ACS Appl. Mater. Interfaces. 10 (2018) 44376–44384. doi:10.1021/acsami.8b13376.

[28] L.L. Zhang, R. Zhou, X.S. Zhao, Graphene-based materials as supercapacitor electrodes, J. Mater. Chem. 20 (2010) 5983–5992. doi:10.1039/c000417k.

[29] F. Shi, D. Xie, Y. Zhong, D.H. Wang, X.H. Xia, C.D. Gu, X.L. Wang, J.P. Tu, Facile synthesis of self-supported Ni2P nanosheet@Ni sponge composite for high-rate battery, J. Power Sources. 328 (2016) 405–412. doi:10.1016/j.jpowsour.2016.08.051.

[30] K. Fic, G. Lota, M. Meller, E. Frackowiak, Novel insight into neutral medium as electrolyte for high-voltage supercapacitors, Energy Environ. Sci. 5 (2012) 5842–5850. doi:10.1039/C1EE02262H.

[31] C. Niu, J. Meng, C. Han, K. Zhao, M. Yan, L. Mai, VO2 nanowires assembled into hollow

microspheres for high-rate and long-life lithium batteries, Nano Lett. 14 (2014) 2873–2878. doi:10.1021/nl500915b.

[32] K.O. Oyedotun, M.J. Madito, A. Bello, D.Y. Momodu, A.A. Mirghni, N. Manyala, Investigation of graphene oxide nanogel and carbon nanorods as electrode for electrochemical supercapacitor, Electrochim. Acta. 245 (2017) 268–278. doi:10.1016/j.electacta.2017.05.150.

[33] O. Ghodbane, J.L. Pascal, F. Favier, Microstructural effects on charge-storage properties in MnO 2-based electrochemical supercapacitors, ACS Appl. Mater. Interfaces. 1 (2009) 1130–1139. doi:10.1021/am900094e.

[34] L. Athouël, F. Moser, R. Dugas, O. Crosnier, D. Bélanger, T. Brousse, Variation of the MnO2 birnessite structure upon charge/discharge in an electrochemical supercapacitor electrode in aqueous Na2SO 4 electrolyte, J. Phys. Chem. C. 112 (2008) 7270–7277. doi:10.1021/jp0773029.

[35] I.I. Misnon, R.A. Aziz, N.K.M. Zain, B. Vidhyadharan, S.G. Krishnan, R. Jose, High performance MnO2 nanoflower electrode and the relationship between solvated ion size and specific capacitance in highly conductive electrolytes, Mater. Res. Bull. 57 (2014) 221–230. doi:10.1016/j.materresbull.2014.05.044.

[36] T.T. Truong, Y. Liu, Y. Ren, L. Trahey, Y. Sun, Morphological and crystalline evolution of nanostructured MNO 2 and its application in lithium-air batteries, ACS Nano. 6 (2012) 8067–8077. doi:10.1021/nn302654p.

[37] K.O. Oyedotun, F. Barzegar, A.A. Mirghni, A.A. Khaleed, T.M. Masikhwa, N. Manyala, Examination of High-Porosity Activated Carbon Obtained from Dehydration of White Sugar for Electrochemical Capacitor Applications, ACS Sustain. Chem. Eng. 7 (2019) 537–546. doi:10.1021/acssuschemeng.8b04080.

[38] W.R. Cannon, B.M. Pettitt, J.A. McCammon, Sulfate anion in water: Model structural, thermodynamic, and dynamic properties, J. Phys. Chem. 98 (1994) 6225–6230. doi:10.1021/j100075a027.

[39] S.H. Lee, Molecular dynamics simulation of ion mobility. 2. alkali metal and halide ions using the spc/e model for water at 25 °c, J. Phys. Chem. 100 (1996) 1420–1425.

doi:10.1021/jp953050c.

[40] K. Zhao, M. Wen, Y. Dong, L. Zhang, M. Yan, W. Xu, C. Niu, L. Zhou, Q. Wei, W. Ren, X. Wang, L. Mai, Thermal Induced Strain Relaxation of 1D Iron Oxide for Solid Electrolyte Interphase Control and Lithium Storage Improvement, Adv. Energy Mater. 7 (2017) 1–10. doi:10.1002/aenm.201601582.

[41] C. Sun, X. Liao, F. Xia, Y. Zhao, L. Zhang, S. Mu, S. Shi, Y. Li, H. Peng, G. Van Tendeloo, K. Zhao, J. Wu, High-Voltage Cycling Induced Thermal Vulnerability in LiCoO2 Cathode: Cation Loss and Oxygen Release Driven by Oxygen Vacancy Migration, ACS Nano. 14 (2020) 6181–6190. doi:10.1021/acsnano.0c02237.

[42] L. Jiang, M. Dong, Y. Dou, S. Chen, P. Liu, H. Yin, H. Zhao, Manganese oxides transformed from orthorhombic phase to birnessite with enhanced electrochemical performance as supercapacitor electrodes, J. Mater. Chem. A. 8 (2020) 3746–3753. doi:10.1039/c9ta12297d.

[43] B. Ming, J. Li, F. Kang, G. Pang, Y. Zhang, L. Chen, J. Xu, X. Wang, Microwave-hydrothermal synthesis of birnessite-type MnO2 nanospheres as supercapacitor electrode materials, J. Power Sources. 198 (2012) 428–431. doi:10.1016/j.jpowsour.2011.10.003.

[44] M. Huang, Y. Zhang, F. Li, L. Zhang, R.S. Ruoff, Z. Wen, Q. Liu, Self-assembly of mesoporous nanotubes assembled from interwoven ultrathin birnessite-type MnO2 nanosheets for asymmetric supercapacitors, Sci. Rep. 4 (2014) 1–8. doi:10.1038/srep03878.

[45] Z. Zhang, C. Ma, M. Huang, F. Li, S. Zhu, C. Hua, L. Yu, H. Zheng, X. Hu, Y. Zhang, Birnessite MnO2-decorated hollow dandelion-like CuO architectures for supercapacitor electrodes, J. Mater. Sci. Mater. Electron. 26 (2015) 4212–4220. doi:10.1007/s10854-015-2969-4.

[46] M.N. Rantho, M.J. Madito, K.O. Oyedotun, D.J. Tarimo, N. Manyala, Hybrid electrochemical supercapacitor based on birnessite-type MnO_2/carbon composite as the positive electrode and carbonized iron-polyaniline/nickel graphene foam as a negative electrode, AIP Adv. 10 (2020) 065113. doi:10.1063/5.0011862.

[47] K.O. Oyedotun, M.J. Madito, D.Y. Momodu, A.A. Mirghni, T.M. Masikhwa, N. Manyala,

Synthesis of ternary NiCo-MnO_2 nanocomposite and its application as a novel high energy supercapattery device, Chem. Eng. J. 335 (2018) 416–433. doi:10.1016/j.cej.2017.10.169.

[48] J.F. Marco, J.R. Gancedo, M. Gracia, J.L. Gautier, E.I. Rios, H.M. Palmer, C. Greaves, F.J. Berry, Cation distribution and magnetic structure of the ferrimagnetic spinel NiCo2O4, J. Mater. Chem. 11 (2001) 3087–3093. doi:10.1039/B103135J.

[49] L. Wang, Z.H. Dong, Z.G. Wang, F.X. Zhang, J. Jin, Layered α-$Co(OH)_2$ Nanocones as Electrode Materials for Pseudocapacitors: Understanding the Effect of Interlayer Space on Electrochemical Activity, Adv. Funct. Mater. 23 (2013) 2758–2764. doi:10.1002/adfm.201202786.